

Influence of Ni and Process Parameters in Medium Mn Steels Heat Treated by High Partitioning Temperature Q&P Cycles



EIDER DEL MOLINO, MARIBEL ARRIBAS TELLERIA, CASEY GILLIAMS, ARTEM ARLAZAROV, JAVIER JESÚS GONZÁLEZ, EMMANUEL DE MOOR, and JOHN GORDON SPEER

In this work, two medium Mn steels (5.8 and 5.7 wt pct Mn) were subjected to a quenching and partitioning (Q&P) treatment employing a partitioning temperature which corresponded to the start of austenite reverse transformation (ART). The influence of a 1.6 wt pct Ni addition in one of the steels and cycle parameters on austenite stability and mechanical properties was also studied. High contents of retained austenite were obtained in the lower quenching temperature (QT) condition, which at the same time resulted in a finer microstructure. The addition of Ni was effective in stabilizing higher contents of austenite. The partitioning of Mn and Ni from martensite into austenite was observed by TEM–EDS. The partitioning behaviour of Mn depended on the QT condition. The lower QT condition facilitated Mn enrichment of austenite laths during partitioning and stabilization of a higher content of austenite. The medium Mn steel containing Ni showed outstanding values of the product of tensile strength (TS) and total elongation (TEL) in the lower QT condition and a higher mechanical stability of the austenite.

<https://doi.org/10.1007/s11661-022-06796-x>
© The Author(s) 2022

I. INTRODUCTION

QUENCHING and partitioning (Q&P) has shown to be a promising heat treatment to produce third-generation advanced high strength steels (AHSSs). In the Q&P process, the steel is first quenched to a temperature between the martensite start (M_s) and the martensite finish (M_f) temperatures, followed by a partitioning treatment designed to enrich the remaining

untransformed austenite with carbon that escapes from the martensite phase. Thereby, carbon stabilized austenite is retained in the microstructure after final quenching to room temperature.^[1] Through this process, a martensitic microstructure with significant content of retained austenite (RA), typically in the range of 5 to 10 pct for low alloy steels,^[2] is obtained. The steel must contain suitable alloying elements to suppress competing reactions during partitioning, such as carbide precipitation,^[3] as well as decomposition of austenite.^[4] Commonly, Si and/or Al are employed to suppress carbide formation, and Mn to reduce bainite formation by *e.g.*, increasing bainite incubation time.^[4,5]

In addition to the Q&P heat treatment, intercritical annealing of medium manganese steels (MMnS) is also considered a promising treatment to produce third-generation AHSSs. In this case, cold rolled martensitic microstructures are intercritically annealed forming austenite by the so-called austenite reverse transformation (ART) phenomenon.^[6] Austenite stabilization can be achieved through diffusion of substitutional elements, such as Mn and Ni, into austenite during high-temperature processing,^[7,8] resulting in rather high contents of RA (20 to 40 pct).^[9–11] The stability of RA and the ultra-fine microstructure in MMnS play a key role in the impressive strength/ductility balance of these steels.^[12–14] Relatively moderate amounts of Mn (4 to 10 pct) are added to promote austenite stabilization.

EIDER DEL MOLINO is with the Tecnalia, Basque Research and Technology Alliance (BRTA), Parque Científico y Tecnológico de Bizkaia, Astondo Bidea, 700, 48160 Derio, Spain and also with the Department of Mining and Metallurgical Engineering University of the Basque Country (ETSI Bilbao UPV/EHU), Calle Alameda Urquijo s/n, 48013 Bilbao, Spain. Contact e-mail: eider.delmolino@tecnalia.com MARIBEL ARRIBAS TELLERIA is with the Tecnalia, Basque Research and Technology Alliance (BRTA), Parque Científico y Tecnológico de Bizkaia. CASEY GILLIAMS, EMMANUEL DE MOOR, and JOHN GORDON SPEER are with the Advanced Steel Processing and Products Research Center, Colorado School of Mines, Golden, CO 80401. ARTEM ARLAZAROV is with the ArcelorMittal Maizières Research SA, Voie Romaine-BP30320, 57283 Maizières-lès-Metz, France. JAVIER JESÚS GONZÁLEZ is with the Department of Mining and Metallurgical Engineering University of the Basque Country (ETSI Bilbao UPV/EHU).

Manuscript submitted March 2, 2022; accepted August 18, 2022.

Article published online September 2, 2022

The main concept of the Q&P process implies the partitioning of carbon from martensite to untransformed austenite by diffusion through martensite/austenite (MA) interfaces. Early assumptions considered an immobile MA interface during partitioning.^[1] However, a later study also included the possible interface migration during partitioning, highlighting the importance of interface migration to adjust the RA fraction and, correspondingly, the austenite carbon content and mechanical stability.^[15] Afterward, several publications experimentally analyzed and modelled the MA interface migration and the formation of austenite.^[16,17] Seo *et al.*^[18] provided direct atomic-scale evidence for the partitioning of both interstitial carbon and substitutional Mn and Si during the Q&P processing of a medium Mn steel with a partitioning temperature of 450 °C. However, in all these previous studies the partitioning temperature was limited to 450 °C and the partitioning of substitutional alloying elements only occurred a few nanometers away from the interface.

Speer *et al.*^[15] presumed that at elevated partitioning temperatures, interface migration was likely to be of greatest importance due to the higher mobility of iron and substitutional alloying elements. Ayenampudi *et al.*^[19] applied high partitioning treatments, in the 400 °C to 600 °C range, to a medium Mn steel. They observed strong competitive reactions (cementite precipitation in austenite films and pearlite formation from blocky austenite), which resulted in a decrease in the fraction of RA with holding time. However, at the highest temperature of 600 °C, high RA volume fractions were obtained in the final microstructure, as a result of austenite reversion and effective austenite stabilization. This result was in line with the work published in Reference 20, though it was also observed that the high RA volume fraction did not result in a significant improvement of mechanical properties, potentially due to the formation of secondary martensite after partitioning and poor mechanical stability of austenite.

In the study conducted in Reference 21, the formation of reverted austenite by reheating the initial primary martensite + pre-existing austenite microstructure to the intercritical region in a Fe–0.2C–8Mn–2Al steel alloy was observed. The new reverted austenite formed during the partitioning stage was enriched with Mn and, hence, was stable during final quenching. The pre-existing austenite grew during partitioning but only the newly formed austenite was enriched in Mn and, therefore, the initial austenite regions transformed into secondary martensite due to the low chemical stability. They also analysed the influence of pre-existing austenite fraction on mechanical properties, observing that an excessive content (30 pct) resulted in coarse secondary martensite which made the material less ductile.

In the present work, high-partitioning temperatures which corresponded to the start of ART were applied. The aim was to promote the formation of austenite and its stabilization by the *partitioning of substitutional alloying elements* and achieve final microstructures with significant amounts of RA. The first quenching step, was, as usual in Q&P, interrupted at a temperature

between M_s and M_f . Thereafter, the formation of austenite by ART from a previous MA microstructure was studied. The high partitioning temperature treatments were applied in a medium Mn steel, designed to increase austenite stabilization by the partitioning of Mn. In contrast to earlier work, here the partitioned substitutional element was not only Mn, but also Ni. Thus, the aim of this study was to investigate the influence of Ni addition and, also, critical process parameters: quenching temperature (QT) and partitioning time (Pt). The effect of Ni addition is less explored compared to Mn, but some recently published results suggest effective austenite stabilization by this element.^[20,22–24] Ni addition was also motivated by its lower segregation in comparison with Mn and because it enhances grain refinement.^[24] The influence of Ni on the transformation of austenite into martensite during interrupted tensile tests was also studied.

Concerning QT (or pre-existing austenite fraction), the influence of this parameter on Mn and Ni partitioning behaviour was investigated, with the aim of better understanding austenite stabilization mechanisms and final tensile properties, which seemed to strongly depend on the initial quenching step. Finally, as concluded in Reference 21, a small fraction of pre-existing austenite could apparently accelerate the austenite reversion kinetics, and, therefore, in the present work, different Pts were also investigated.

II. MATERIALS AND METHODS

Two different MMnS sheets, with composition shown in Table I, were produced in the laboratory using a vacuum induction melting furnace. In one of the steels Ni was added (hereafter MnNi steel) and the other steel was Ni free (hereafter Mn steel). The ingots were reheated to ~ 1250 °C and a roughing stage was first performed to decrease the thickness from 60 to 30 mm. The slabs were then cut into five smaller pieces which were hot rolled after being reheated to ~ 1250 °C. The hot rolling consisted of five hot rolling passes (end temperature of rolling approximately above 900 °C) and coiling at 500 °C. The hot rolled sheets of about 4 mm thickness were ground on both surfaces to decrease the thickness to 2.8 mm. Then, the sheets were cold-rolled with approximately 50 pct reduction to obtain a final thickness of 1.5 mm. A softening anneal was applied before cold rolling which consisted of holding at 600 °C for 1 hour followed by water quench.

Phase transformation temperatures (A_{c1} , A_{c3} , M_s , M_f) and QTs corresponding to 10 pct and 25 pct of pre-existing austenite (QT10 and QT25, respectively) were determined by means of a LINSEIS L78 RITA dilatometer, using cylindrical samples with 3 mm diameter and 10 mm length. First, the A_{c1} and the A_{c3} temperatures were determined by heating the samples at 5 °C/s up to 1000 °C. For the determination of the M_s and the QTs, the samples were heated at 5 °C/s to 50 °C above the A_{c3} and held for 120 seconds. Afterward, samples were cooled down to room temperature by employing a cooling rate of 20 °C/s, and then were

reheated up to 500 °C at 5 °C/s. The applied cooling rate was above the critical cooling rate for avoiding diffusion-based phase transformations, which were experimentally determined in advance for both steels by means of dilatometer experiments, being < 0.1 °C/s for both steels. Dilatometry curves during quenching from $A_{c3} + 50$ °C to room temperature were used to determine the M_s temperatures. Martensite transformation curves were determined by applying the lever rule between the expansion of the untransformed austenite curve and from reheating to 500 °C. Thus, QTs that corresponded to 10 and 25 pct of pre-existing austenite were determined.

Additionally, the temperature for the start of ART (T_{ART}) upon heating from the QT was determined by dilatometry. For this, samples were heated to $A_{c3} + 50$ °C, held for 120 s, cooled down as previously described to QT25 and QT10, and re-heated again up to $A_{c3} + 50$ °C. It was shown that T_{ART} was very similar between reheating from QT25 and QT10. Resulting values are summarized in Table II.

Q&P cycles with QT25 and QT10 QTs, partitioning at T_{ART} and Pts ranging from 300 to 3600 seconds were applied to each steel. The selection of T_{ART} as partitioning temperature was motivated from previous work,^[20] in which it was observed that temperatures beyond the intercritical range lead to undesirable decomposition of austenite into pearlite. Higher partitioning temperatures might also lead to excessive austenite which would be difficult to stabilize. Cycle parameters are shown in Table III and schematically represented in Figure 1. The aim of employing different Pts in the QT10 condition was to investigate the kinetics of austenite transformation with a small fraction of pre-existing austenite present before partitioning. The Q&P cycles were performed on flat samples with 125 × 20 × 1.4 mm dimensions in furnaces using an Ar atmosphere. The first heating to $A_{c3} + 50$ °C was carried out in a furnace. It was found that air cooling was sufficient to exceed the critical cooling rate and thereby avoid unwanted transformations. Therefore, samples were air cooled down to the corresponding QT

and reheated up to partitioning temperature in a second furnace. Finally, once the desired Pt was completed, samples were water quenched. Temperature evolution was monitored during the thermal treatments and, afterward, the monitored cycles were reproduced in the dilatometer.

X-ray diffraction (XRD) measurements were carried out on the Q&P treated samples using a diffractometer equipped with a Cr $K\alpha$ anode, PolyCap™ and LynxEye fast detector. The samples for XRD were prepared by conventional mechanical polishing to 1 μm. RA content was obtained according to the ASTM E975-13 standard.

Electron backscatter diffraction (EBSD) scans were performed on a field emission scanning electron microscope (FE-SEM, JEOL® JSM7000F) with a beam voltage of 20 kV and a medium probe current. The acquisition of EBSD scans was done using a step size of 0.06 μm. Selected samples were prepared for metallography by conventional polishing to 1 μm, followed by final polishing with colloidal silica. After initial analysis using the TSL/OIM Data Analysis software package, a neighbor CI correlation clean-up using a minimum confidence index of 0.1 was performed. Grain size was adjusted using a grain tolerance angle of 5 deg, a minimum size (points) of 3 for grains and 2 for anti-grains. Samples for SEM observation were etched with 2 pct Nital for 30 seconds and a beam voltage of 15 kV, a medium probe current, and a working distance of 10 mm were employed. Further microstructure characterization was done by means of a transmission electron microscope (TEM, Talos F200i field emission gun instrument equipped with a Bruker X-Flash100 XEDS spectrometer). Elemental maps were obtained by XEDS in the STEM mode under a high annular dark field (HAADF) detector for Z contrast imaging in STEM conditions (camera length of 160 mm) using a pixel size of 2 nm, a dwell time of 900 seconds and an image size of 512 × 512 pixels. For this, 3 mm diameter discs were thinned to 80 to 100 μm by mechanical polishing and then electropolished at room temperature (20 °C) using a 5 pct perchloric acid and 95 pct ethanol solution. The polishing potential was 29 V at a current of 100 mA.

Room-temperature tensile tests were performed employing a standard geometry of 50 mm gauge length, in a universal INSTRON tensile testing machine, with a strain rate of 0.001 s⁻¹ and a contact extensometer. Interrupted tensile tests were also performed in order to assess the evolution of the RA under mechanical loading. For that, the tensile tests were stopped at the selected strain. Then, the deformed area of the tensile specimen was selected and, after preparing the surface

Table I. Chemical Composition of the Investigated Steels (Wt Pct)

Steel	Composition (Wt Pct)						
	C	Si	Mn	Ni	P	S	N
Mn	0.19	1.4	5.8	0.0	0.011	0.0013	0.0033
MnNi	0.19	1.4	5.7	1.6	0.014	0.0019	0.0041

Table II. Experimental Phase Transformation Temperatures, Quenching Temperatures Corresponding to 10 and 25 pct of Pre-existing Austenite (QT10 and QT25) and Temperatures for the Start of Austenite Reverse Transformation (T_{ART})

Steel	A_{c1} (°C)	A_{c3} (°C)	M_s (°C)	M_f (°C)	QT10 (°C)	QT25 (°C)	T_{ART} (°C)
Mn	695	841	252	< RT	60	148	660
MnNi	690	793	219	< RT	44	114	640

by mechanical polishing, the RA fraction was measured by XRD in the same aforementioned way.

III. RESULTS

A. Dilatometry Curves of the Q&P Heat Treatments

Dilatometry curves obtained by the simulation of the complete Q&P cycle are represented in Figures 2(a) and (b) for each thermal cycle applied to the Mn and MnNi steels. The relative change in length measured during the partitioning stage is presented for both the Mn and MnNi steels in Figures 3(a) and (b), respectively, considering Pt1000 cycles for both QT conditions. In the latter figures, a continuous contraction of the samples during partitioning was observed in all cases, which can be related to the formation of reverted austenite. These curves reveal that equilibrium conditions were not reached in the austenite formation reaction in any of the conditions, since contraction had not yet reached a plateau. Moreover, in the QT10 condition the contraction was greater than in the QT25 condition, particularly in the Mn steel. The reverted austenite formed during partitioning was calculated using the lever-rule and it is shown in Figures 3(c) and (d). It can be observed that the QT10 condition resulted in a greater increase in the reverted austenite percentage during partitioning, and thus faster austenite formation kinetics.

The dilatometry curves during final cooling to room temperature were analyzed to study the possible formation of secondary martensite (Figure 2). The curve was linear in all QT10 conditions and in both steels, which means that the formation of secondary martensite was not significant and, therefore, most of the austenite (pre-existing + reverted) available at the end of partitioning was retained in the final microstructure. In this sense, the QT10 condition seemed to be beneficial to stabilize austenite. In contrast, for the QT25 condition, the dilation curves deviated from linear contraction, which denoted secondary martensite transformation during final cooling. The secondary martensite transformation temperatures (M_s^2) were determined to be 103 °C and 57 °C in the Mn and MnNi steels, respectively. The lower M_s^2 temperature observed in the MnNi steel indicated that austenite stabilization was enhanced, which was likely due to the known stabilization capacity of Ni.^[20,22–24]

B. Microstructure After Q&P Cycles

The RA contents measured by XRD are shown in Figure 4. All the cycles resulted in a final RA content greater than the pre-existing austenite content at the QT. In the case of the QT25–Pt1000 cycle applied to the Mn steel, the increase in austenite content with respect to the pre-existing amount was small, however, in all other conditions, a very substantial increase was observed. The maximum content of RA was 47 pct, which was obtained after the application of the QT10–Pt1000 cycle in the MnNi steel.

The Ni addition clearly resulted in a significant increase in RA content, regardless of the thermal treatment conditions. Furthermore, comparing the QT25–Pt1000 and the QT10–Pt1000 conditions, it can be seen that a lower pre-existing austenite content at the QT clearly resulted in an increased content of RA in the final microstructure of both steels. As to the influence of Pt in the QT10 condition, increasing the Pt from 300 to 1000 seconds also increased the RA content. However, a further increase to 3600 seconds resulted in a slight decrease in RA content. The influence of Pt on RA content was very similar for both steels.

The microstructure expected in these samples can be described as follows: after heating to obtain a fully austenitic microstructure, the Q&P steels were quenched to the predetermined QT in order to form a partially austenitic and partially martensitic microstructure.^[25,26] Then, heating to a partitioning temperature, which corresponded to the austenite reversion transformation start temperature, the pre-existing austenite was expected to grow and be enriched by Mn and C provided by the martensite.^[5,27] Thus, after final quenching, the austenite which contained enough C and Mn would become stable and be retained at room temperature,^[5,27] whereas the less enriched austenite would transform into secondary martensite (α'_{sec}). In this way, the expected final microstructure should consist of C and Mn depleted primary martensite (M1), RA laths and blocky RA, and MA islands consisting of secondary martensite with fine RA. Carbide precipitation was also expected as a result of the tempering of martensite due to the high partitioning temperature employed.

In the FE-SEM micrographs obtained in the present work, bright thin films were observed in all micrographs, which were likely RA. The dark phase is interpreted to be primary martensite (M1) containing a considerable

Table III. Q&P Cycle Parameters Applied to the Mn and MnNi Steels

Q&P Cycle	Mn Steel			MnNi Steel		
	QT (°C)	PT (°C)	Pt (s)	QT (°C)	PT (°C)	Pt (s)
QT25–Pt1000	148	660	1000	114	640	1000
QT10–Pt300	60	660	300	44	640	300
QT10–Pt1000			1000			1000
QT10–Pt3600			3600			3600

amount of carbides. The carbides exhibited both acicular/plate and globular morphologies. Mn retards cementite dissolution, so observed carbides could include some cementite that did not dissolve in prior steps, along with cementite formed as a consequence of tempering of the martensite. The regions with dark-grey center and white edges are generally recognized as MA islands. In the QT25–Pt1000 micrographs large areas of MA are evident. However, as shown later, the amount of secondary martensite determined from the dilatometry curves and XRD results was not a significant

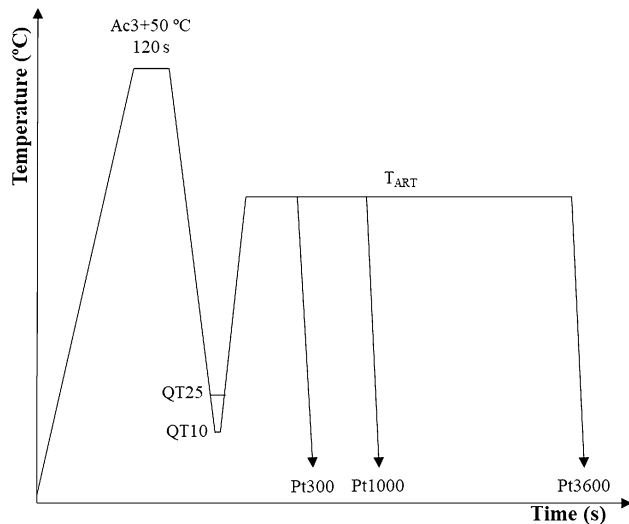


Fig. 1—Schematic of the Q&P cycles applied in this work.

quantity. Therefore, the interpretation of these areas in the FE-SEM images is not entirely clear, but is presumably indicative of transformation during cooling near QT. In both steels, the microstructure observed after the QT25–Pt1000 cycle presented coarse and blocky constituents, whereas after the QT10–Pt1000 cycles the microstructure was thinner and exhibited a lath-type appearance. The microstructure features in the MnNi steel after the QT10–Pt3600 cycle (Figure 5(e)) were thinner than after the QT25–Pt1000 cycle, but coarser than after the QT10–Pt1000 cycle.

EBSD phase maps were obtained for all the Pt1000 conditions. EBSD phase maps obtained after the neighbor CI correlation clean-up are shown in Figure 6, where the red phase was identified as RA, green is martensite, and black indicates unidentified regions. From EBSD measurements, RA content and size were obtained. In Table IV a comparison between the RA content measured by XRD and EBSD is shown. The RA content measured by EBSD was lower than that measured by XRD, which might be due to three reasons: first, the dark regions in the EBSD maps can be MA islands containing RA. However, these regions are mostly recognized as unidentified regions. Second, it should be noted for FE-SEM, the maximum resolution that can be attained in EBSD analysis is on the order of 100 nm^[28] and thus, EBSD does not resolve thin austenite films or austenite grains smaller than 100 nm in diameter or thickness. Third, the area and depth of the samples that were analyzed in XRD and EBSD are different. The percentages of the unidentified points and a comparison between maps before and after the

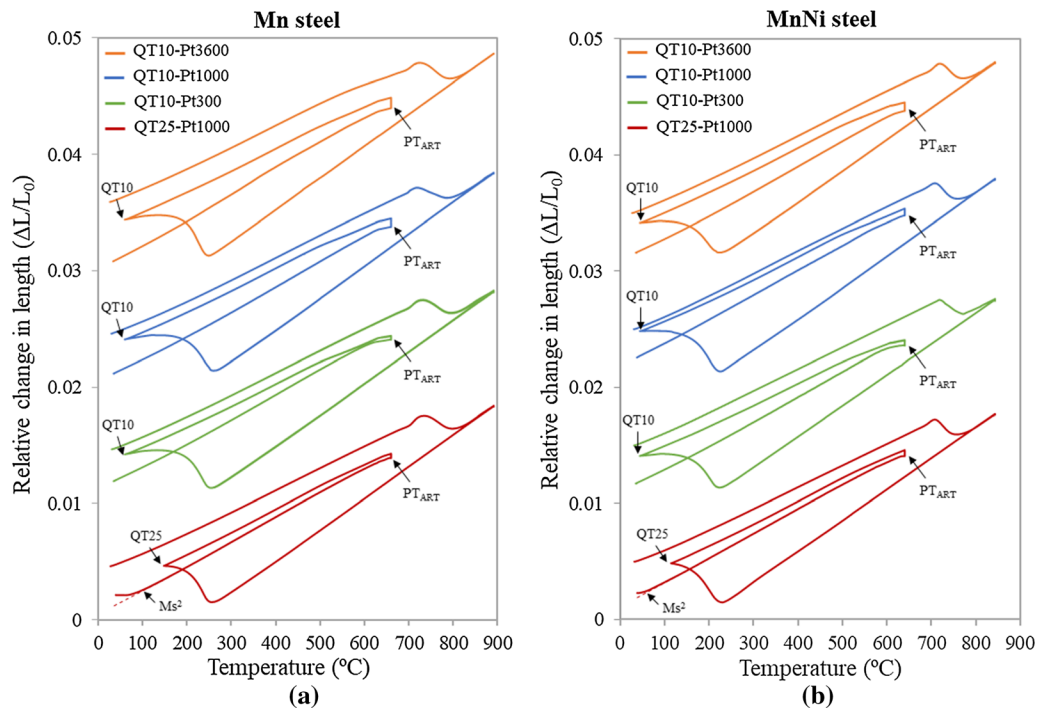


Fig. 2—Dilatometry curves of the applied Q&P cycles: (a) Mn steel, and (b) MnNi steel. The curves corresponding to the QT25 and Pt1000 condition, and the QT10 and Pt300, Pt1000 and Pt3600 conditions, are shown for both steels, considering in all cases a partitioning temperature corresponding to the start of ART.

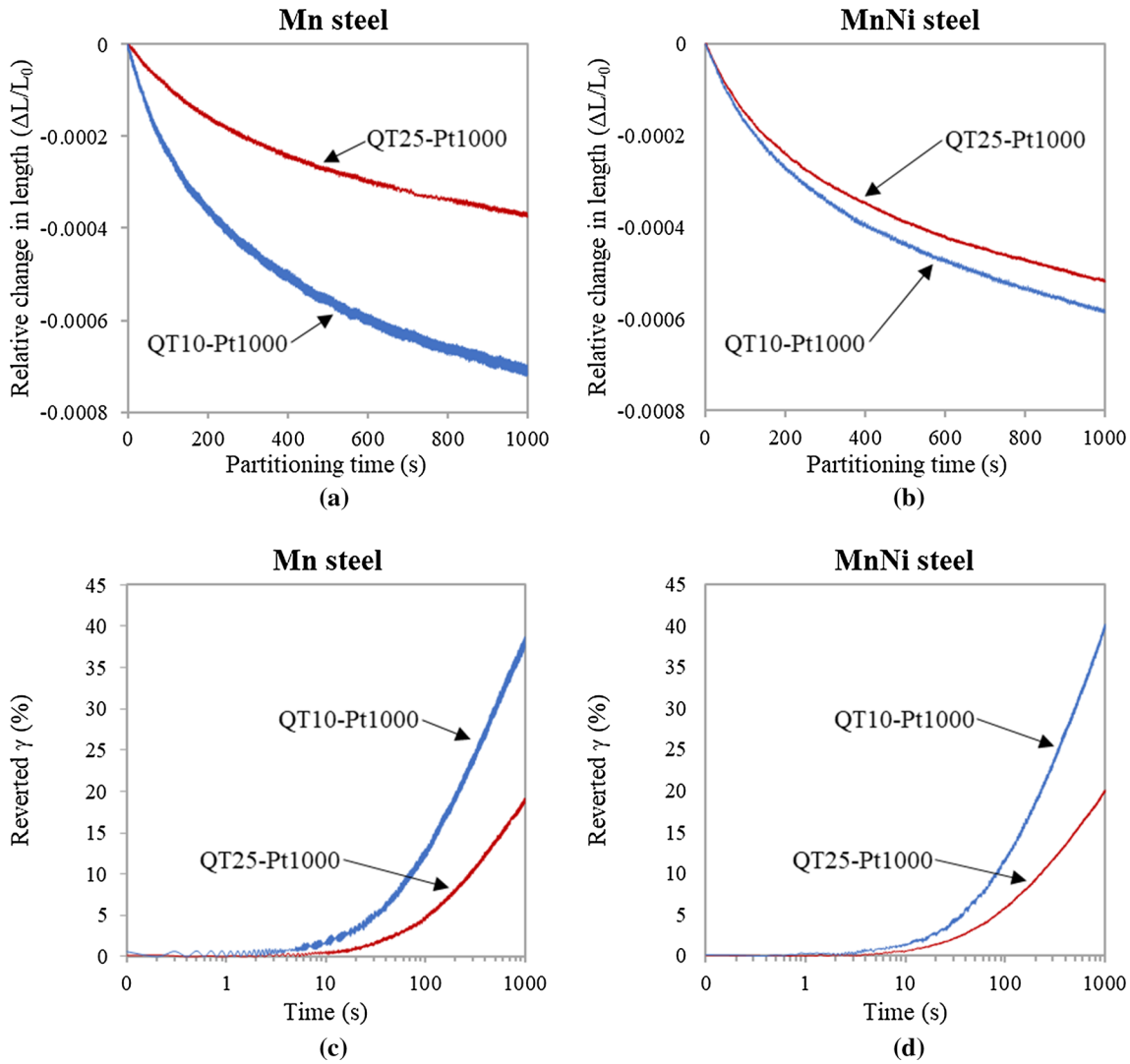


Fig. 3—Relative change in length measured during the partitioning stage for the QT10–Pt1000 and the QT25–Pt1000 cycles: (a) Mn steel and (b) MnNi steel. Evolution of the reverted austenite during the partitioning in the QT10–Pt1000 and the QT25–Pt1000 cycles in the Mn (c) and MnNi (d) steels.

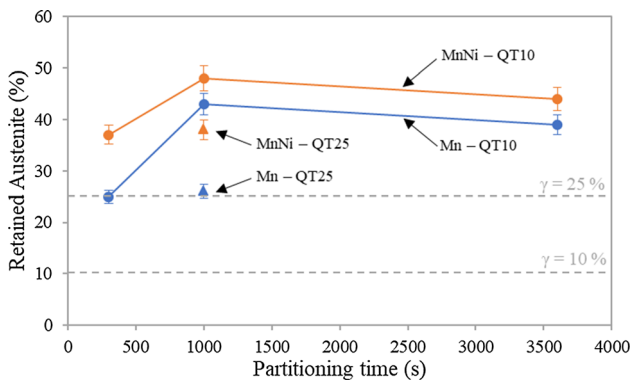


Fig. 4—Retained austenite content as a function of partitioning time measured after the application of all Q&P cycles.

neighbor CI clean-up of the Mn steel and QT25–Pt1000 condition as an example are summarized in Table S-1 and Figure S-1, respectively (refer to Electronic

Supplementary Material data file). Most of the dark zones in the QT25 cycles (Figures 6(a) and (b)) likely corresponded to secondary martensite, as the dislocation density was high in these regions, whereas the thin dark zones between martensite areas in the QT10 condition (Figures 6(c) and (d)) likely included nanometer sized film-like RA. In Table IV, average RA sizes as well as the standard deviation (SD) values estimated from EBSD measurements are also shown. In the Mn steel, the QT10–Pt1000 condition resulted in a coarser average RA size in comparison with the QT25–Pt1000 condition. However, as mentioned above, EBSD does not resolve thin films below a minimum austenite size of about 100 nm and fine scale film-like RA areas were mostly not detected in the measurement. On the other hand, even without considering grains smaller than 100 nm, the high SD values reveal that the distribution of the RA grain size was not homogeneous.

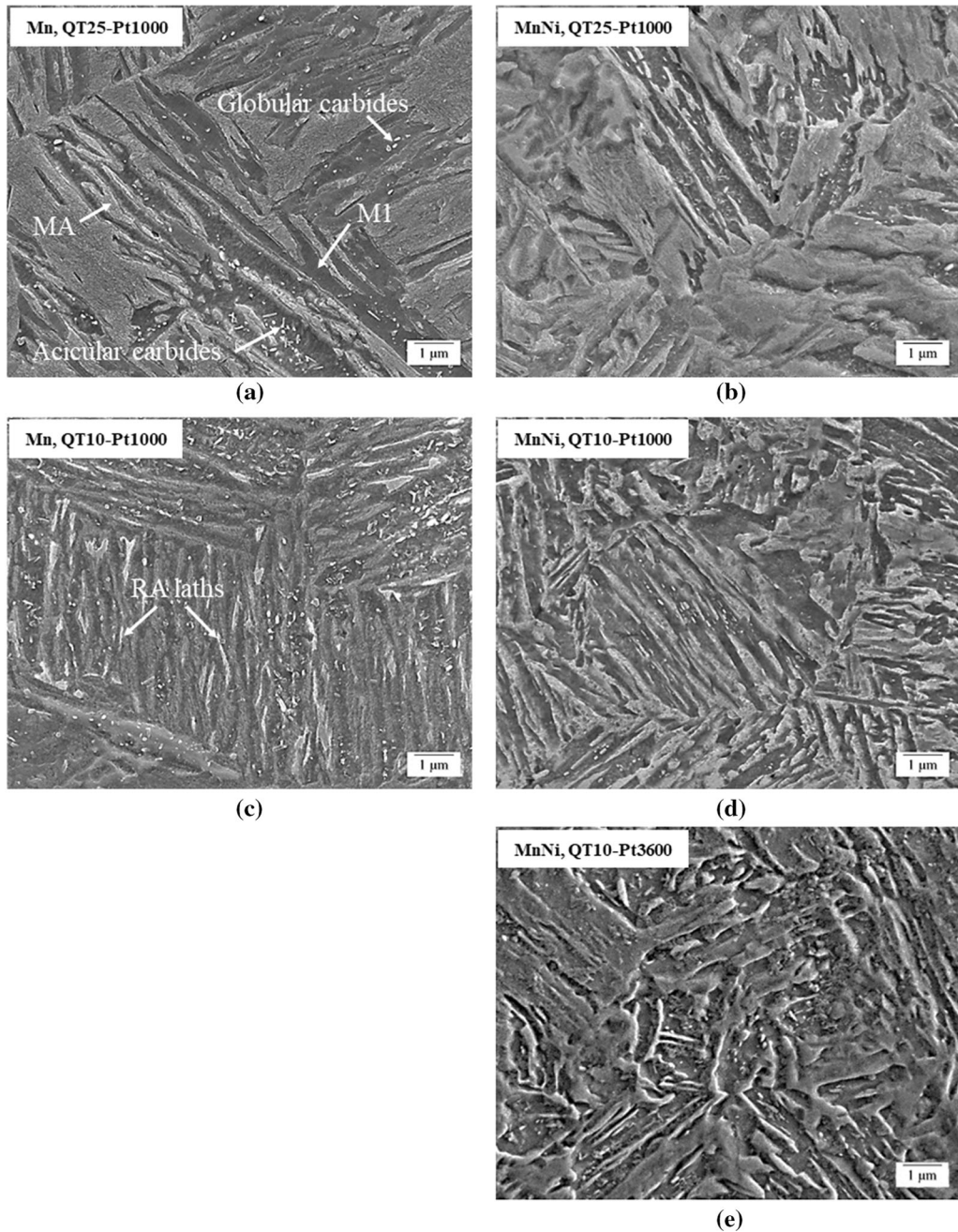


Fig. 5—FE-SEM micrographs corresponding to the QT25–Pt1000 cycle for the Mn (a), and MnNi (b) steels; the QT10–Pt1000 cycle for the Mn (c), and MnNi (d) steels; and the QT10–Pt3600 cycle for the MnNi steel (e).

In Figure 7, TEM characterization results are presented for the MnNi steel. Figures 7(a) and (b) show TEM micrographs after the application of the QT25–Pt1000 and QT10–Pt1000 cycles, respectively. In both cases, the microstructure consisted of lath-type constituents which were identified as martensite and austenite by means of selected area diffraction (SAD). Carbides were also observed, and their characterization is described later. In general, the austenite and martensite laths appeared thinner in the QT10–Pt1000 condition. Moreover, a large number of laths were thinner than the detection limit employed in EBSD analysis

(~ 100 nm). The laths identified as austenite in the QT25–Pt1000 condition had a width of 53 ± 5 nm, explaining the lower RA contents measured by EBSD in comparison with XRD measurements.

With the aim of understanding the partitioning behaviour of Mn and Ni, TEM–energy dispersive spectroscopy (EDS) analysis was performed and the compositional maps (Figures 7(c) through (f)) and concentration profiles (Figures 7(g) and (h)) were obtained for Mn and Ni alloying elements. The compositional maps revealed that the Mn concentration was not homogeneous, with austenite films enriched in this

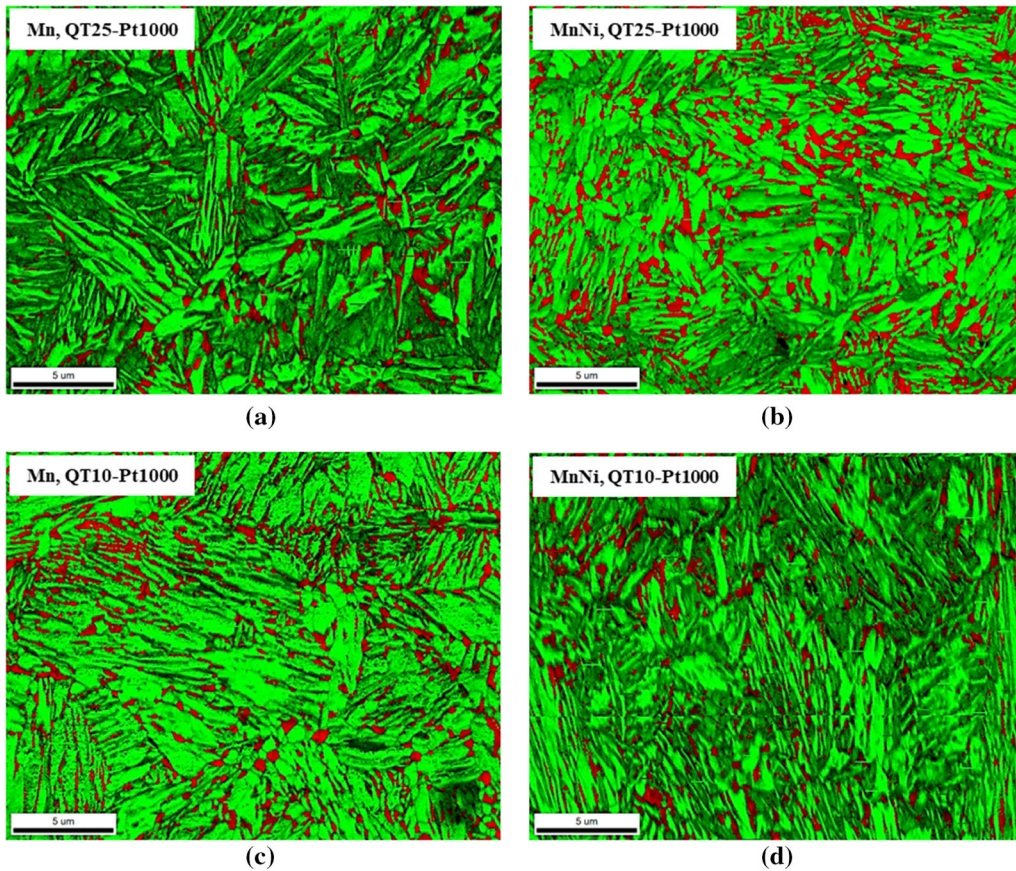


Fig. 6—EBSD scans corresponding to the QT25–Pt1000 cycle for the Mn (a), and MnNi (b) steels; and the QT10–Pt1000 cycle for the Mn (c), and MnNi (d) steels (Color figure online).

element. On the contrary, Ni concentration was more homogeneous. The concentration profiles obtained for the QT25–Pt1000 condition (Figure 7(g)), revealed high-Mn enrichment in the region identified as austenite by SAD, obtaining a maximum concentration of 15 wt pct, and a lower Mn concentration in the laths identified as martensite. In the latter, Mn content was around the nominal value (grey laths) or above this value (white laths), and consequently, the laths were deduced to be primary and secondary martensite, respectively. Likely, pre-existing austenite laths at QT25 were too large to be completely enriched in Mn and, as a consequence, a Mn gradient was observed between the pre-existing austenite boundary and lath center. Hence, secondary martensite transformed from the interior of the austenite films remaining from cooling to the QT, originating MA islands in the final microstructure.^[21,29] On the contrary, in the QT10 condition (Figure 7(h)) a higher percentage of the lath was enriched in Mn and the concentration profile was more homogeneous. Furthermore, the Mn concentration in the enriched laths was significantly higher than in the QT25 condition. Therefore, it can be concluded that in the high partitioning temperature Q&P cycles applied in this work, Mn partitioning occurred and the lower QT condition was beneficial for the Mn enrichment of austenite laths, which likely contributed to austenite stabilization. Ni concentration profiles did not show such clear concentration

differences between laths as those of Mn, but Ni partitioning was more noticeable for the QT10–Pt1000 cycle. The effect of Ni is further discussed in Section IV–B.

C. Tensile Properties

Figure 8 shows stress–strain curves for all Q&P cycles and both steels. All data obtained from the tensile tests are summarized in Table V. All tensile strength (TS) values exceeded 1150 MPa. These values were higher for the QT25–Pt1000 cycles. In the QT10 cycles, a small rise in TS was shown by increasing Pt, as well as by the Ni content addition to the alloy. The influence of Ni on TS was more noticeable in the QT25 cycle. The yield strength (YS) was higher for the QT10 cycles, although, the YS/TS ratio was quite low in all cases. Stress–strain curves revealed good global formability (tensile ductility) in both steels, particularly for the QT10 cycles. However, post-uniform elongation was limited and, in the case of the QT25 cycles, fracture occurred before necking. In addition, discontinuous yielding was observed after the QT10 cycles with serrations present at long Pts (1000 and 3600 seconds).

When it comes to total elongation (TEL), different levels were obtained depending on the Q&P cycle parameters. The influence of QT on tensile curves was clearly visible, resulting for the QT10 cycles in a

Table IV. Comparison Between Retained Austenite Content (RA Pct) Measured by XRD and EBSD

Q&P Cycle	Mn					MnNi			
	XRD (RA Pct)	(RA Pct)	EBSD (RA Pct)	EBSD (RA nm)	SD (nm)	XRD (RA Pct)	EBSD (RA Pct)	EBSD (RA nm)	SD (nm)
QT25–Pt1000	26		13.3	219	138	38	23.1	276	188
QT10–Pt1000	43		18.6	307	174	48	13.1	220	147

Average retained austenite grain size (RA nm) and SD measured by EBSD.

notable increase of the TEL values in both steels. In the QT10 cycles, the influence of Pt on TEL depended on the steel: in the Mn steel, TEL reached its maximum value, 24.9 pct, with a Pt of 1000 seconds. In the MnNi steel, TEL increased with Pt, achieving a TEL of 28.8 pct in the cycle with a Pt of 3600 seconds. It was also observed that the addition of Ni was beneficial for increasing TEL.

The product of tensile strength and total elongation ($TS \times TEL$) was clearly different depending on the QT condition. Outstanding values were obtained after QT10 cycles, particularly in the MnNi steel with Pts of 1000 and 3600 seconds, which resulted in 33.8 and 35.2 GPa pct, respectively (Figure 9). The distinctive behaviors in the QT25 conditions reflected the increased presence of secondary martensite.

D. Interrupted Tensile Tests

Figure 10 shows the results of the interrupted tensile tests performed after the application of the QT10–Pt1000 cycle in both steels. The figure provides the RA values obtained after different strain levels and the corresponding stress–strain curve. The evolution of RA with strain was different in the Mn compared to the MnNi steels. In the Mn steel, the RA slightly decreased from 43 to 38 pct after applying a strain of 5 pct, then, remained almost steady up to a strain of 10 pct and, afterward, considerably decreased down to 16 pct at an elongation of 15 pct. Finally, after final fracture, no austenite was measured. In the MnNi steel, by contrast, a small near linear decrease of RA was observed up to 20 pct elongation, from 48 to 37 pct; then, a full transformation of remaining RA occurred when the sample fractured at 28 pct elongation. These results indicate an increase in austenite stability for the MnNi steel.

IV. DISCUSSION

A. Influence of Heat Treatment Parameters on Austenite Stabilization

A clear influence of QT and Pt on the final microstructure and degree of austenite stabilization was observed in this work. The lower QT applied, QT10, resulted in faster austenite formation kinetics in the partitioning stage (as denoted by the higher contraction observed in the partitioning stage, Figure 3), less formation of secondary martensite during final

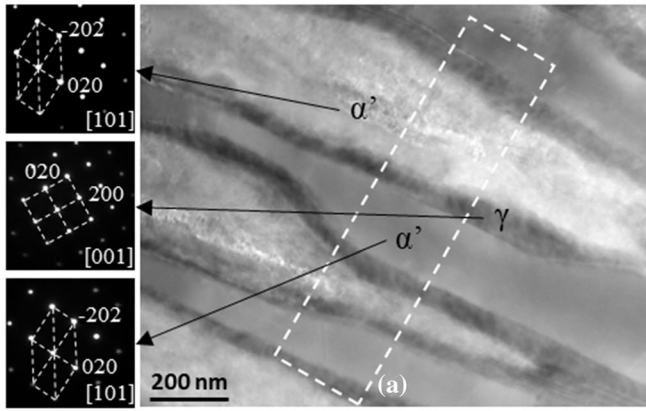
cooling, and a final microstructure with a higher content of RA, which, at the same time, showed a lath-type microstructure with finer constituents. Therefore, preserving 10 pct of pre-existing austenite in the quenching step (QT10 condition) was beneficial for austenite stabilization, as well as for enhancing microstructure refinement.

The faster kinetics observed for the QT10 condition were in agreement with the results reported in Reference 24, where it was also reported that the amount of reverted austenite increased while the amount of pre-existing austenite decreased. At lower QTs, it can be expected that the formation of fine martensite laths separates pre-existing austenite into smaller sizes. Liu *et al.*^[30] found that pre-existing austenite lath size strongly decreased with decreased QT. Therefore, in the present work, it is likely that in the QT10 condition the initial MA microstructure was finer and, consequently, more nucleation/growth sites were available for austenite formation accelerating the kinetics of the reaction, and the diffusion distances for substitutional solute redistribution were accordingly reduced.

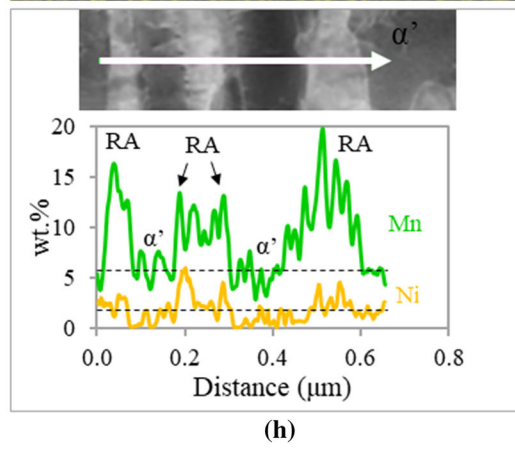
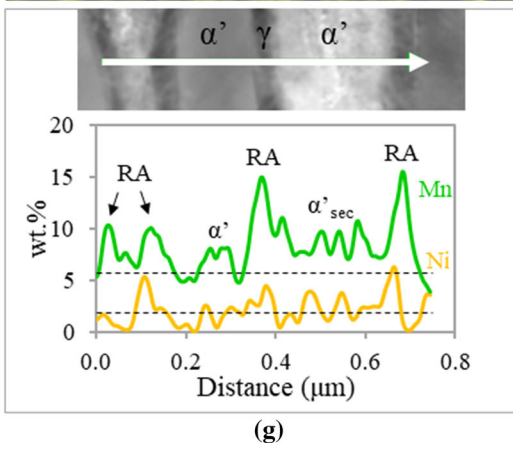
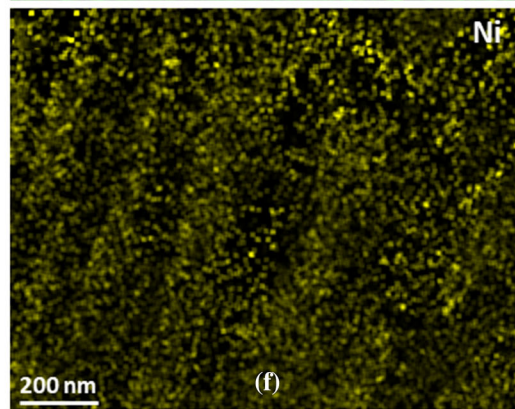
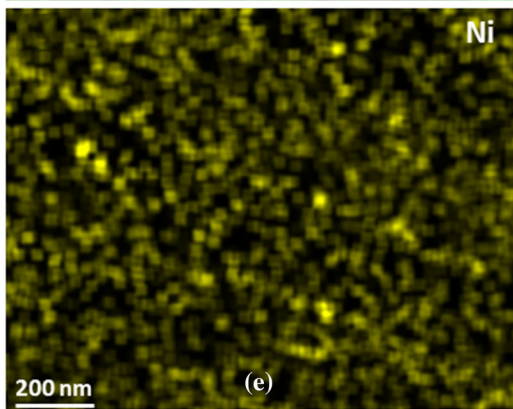
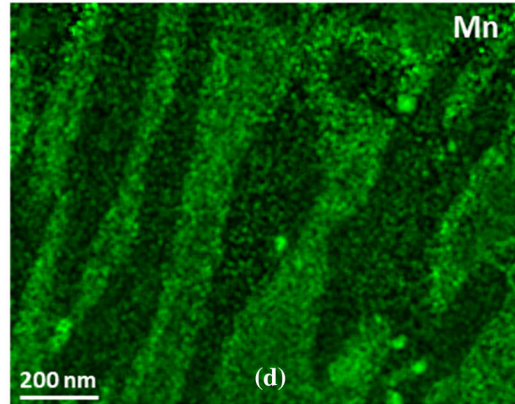
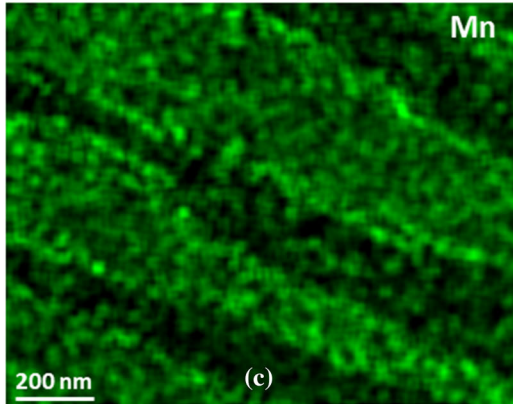
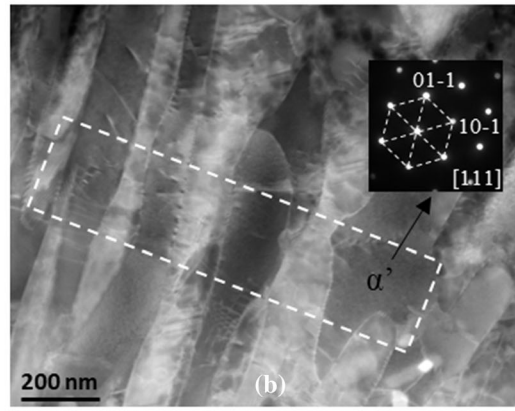
As previously mentioned, the lower QT condition was beneficial for austenite stabilization. The Mn partitioning between martensite and austenite was expected to play a key role in the austenite stabilization. Many publications on intercritically annealed medium Mn steels, show that Mn partitioning occurs between ferrite and austenite contributing to stabilize high amounts of austenite.^[7,8] Although long soaking times are commonly reported for this partitioning to occur,^[5,12,31] some investigations demonstrate that Mn partitioning occurs also in short annealing periods.^[32] De Moor *et al.*^[33] suggested that the high density of dislocations and the grain boundaries should facilitate Mn diffusion. Therefore, some Mn partitioning was expected, which, additionally, was likely facilitated by the small size of pre-existing austenite grains in the QT10 condition due to the shorter diffusion paths.

In this work, Mn partitioning was characterized by means of TEM–EDS analysis, and the extent of partitioning was different depending on the employed QT. Thus, thermal stability of austenite at the end of the partitioning in MnNi steel was analyzed for the QT10–Pt1000 and QT25–Pt1000 conditions. For this, the local M_s was calculated by the Andrews equation^[34] (Eq. [1]) for the laths where TEM–EDS line scans were performed in Figure 7 (two and three laths for the QT25 and QT10 conditions, respectively) and, then the

MnNi, QT25-Pt1000



MnNi, QT10-Pt1000



◀Fig. 7—TEM analysis of the MnNi steel: micrographs and SAD patterns for the QT25 (a) and the QT10 (b) conditions; EDS analysis representing the distribution of Mn concentration for the QT25 (c) and QT10 (d) conditions, and Ni concentration for the QT25 (e) and QT10 (f) conditions; profiles of Mn and Ni line scans for the QT10 (g) and QT25 (h) conditions.

Koistinen–Marburger equation^[35] (Eq. [2]) was applied to obtain the corresponding RA volume fraction.

$$M_s = 539 - 423C - 30.4Mn - 17.7Ni - 11.0Si - 12.1Cr - 7.5Mo, \quad [1]$$

where the alloying elements are expressed in weight percent.

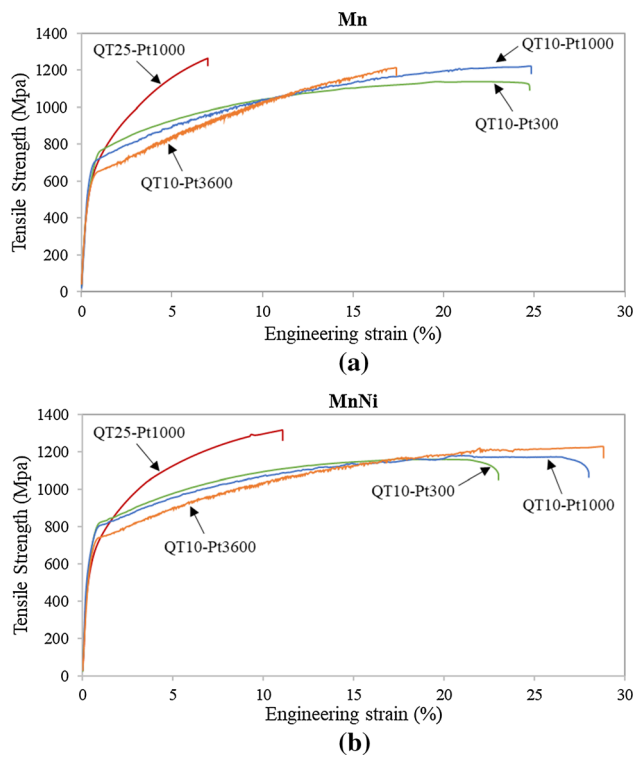


Fig. 8—Engineering stress–strain curves obtained after Q&P treatments for the Mn (a) and MnNi (b) steels.

$$f_\gamma = \exp(-0.011 \times (M_s - T)), \quad [2]$$

where f_γ is austenite volume fraction, and T is current temperature in °C.

Finally, the RA percent was calculated by integrating under the curve of local stable austenite fraction.^[36] Values for Mn, Ni and Si were taken from TEM–EDS line scans, while the employed C content was considered the ortho-equilibrium value (0.003 wt pct for the martensite and 0.326 wt pct for the austenite), obtained using Thermo-Calc. The QT10 condition led to a higher stability of austenite after partitioning. Calculations showed that an average of 82 pct of the austenite present at the end of partitioning (pre-existing + reverted) was stabilized to room temperature. Thus, given that the measured RA in the final microstructure of this steel was 48 pct, the total amount of austenite at the end of partitioning would be estimated to be ~ 58 pct, considering that 82 pct of the austenite present at the end of partitioning was stabilized. Hence, the amount of secondary martensite formed during final cooling would also be approximately 10 pct. In the case of the QT25 condition, at the end of partitioning, only an average of 54 pct of the pre-existing + reverted austenite was sufficiently stable to avoid transformation during final cooling. The RA content in the final microstructure was

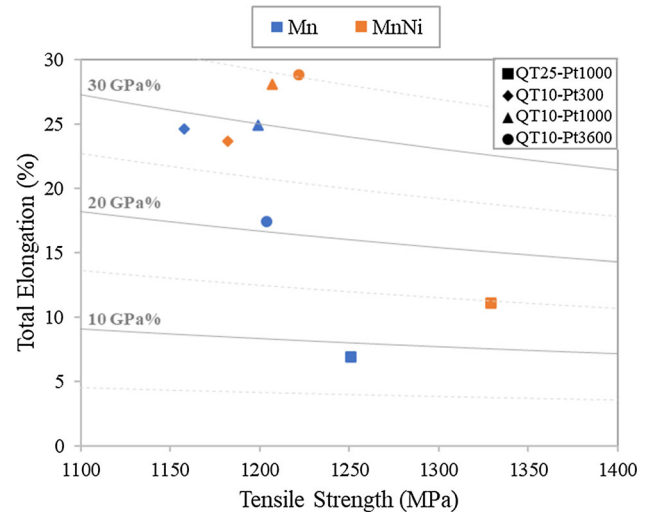


Fig. 9—Relationship between total elongation (pct) and tensile strength (MPa) obtained after Q&P cycles in Mn and MnNi steels.

Table V. Summary of Tensile Properties for the Mn and MnNi Steels After Each Q&P Treatment

Steel	Q&P Cycle	YS (0.2 Pct Offset) (MPa)	TS (MPa)	YS/TS Ratio	TEL (Pct)	TS × TEL (GPa Pct)
Mn	QT25–Pt1000	585	1251	0.47	6.9	8.6
	QT10–Pt300	644	1158	0.56	24.6	28.5
	QT10–Pt1000	651	1199	0.54	24.9	29.9
	QT10–Pt3600	584	1204	0.48	17.4	20.9
MnNi	QT25–Pt1000	580	1329	0.44	11.1	14.7
	QT10–Pt300	727	1182	0.61	23.7	28.0
	QT10–Pt1000	694	1207	0.57	28.1	33.8
	QT10–Pt3600	705	1222	0.58	28.8	35.2

38 pct; thus, at the end of partitioning it would be 70 pct, indicating that the secondary martensite content in this steel would be around 32 pct, formed mainly inside the coarse austenite laths, where the Mn content was considerably lower than near the boundaries.

These estimated secondary martensite fractions are considerably higher than would be expected from the dilatometry curves (Figure 2), suggesting that other parameters, apart from composition influenced the thermal stability of the austenite. Arlazarov *et al.*^[37] investigated the role that grain size plays in thermal stability of austenite in a MMnS and they found that a grain size smaller than 0.5 μm clearly lowered the M_s , increasing austenite stability. In the previous calculations of M_s and final RA amount, the effect of grain size was not considered, however, the microstructures presented in this work showed average grain sizes smaller than 0.5 μm , which likely implies that the thermal stability of the austenite was higher than the values presented above, especially in QT10 condition. The Pts employed in the present work were significantly lower than those sometimes employed in the intercritical annealing of medium Mn steels (hours). However, the RA contents, particularly in the QT10 condition, were similar.^[12–14] In Reference 38 the authors studied austenite growth during intercritical annealing from as-quenched martensite containing interlath RA. They concluded that austenite grew from thin austenite films between laths retained upon quenching, but also nucleated at martensite lath boundaries, packet boundaries, and within laths. Similar results were obtained in

Reference 21, where it was also concluded that the fact that the pre-existing austenite could grow directly without nucleation would enhance the kinetics of austenite reversion. This means that the time needed for the austenite reversion would decrease and may explain the high RA fractions obtained in the present work employing significantly lower Pts.

The influence of Pt on the final RA content was evident (Figure 4). In both steels, RA content increased significantly by increasing the Pt from 300 to 1000 seconds. However, a further increase to 3600 seconds resulted in a reduction of RA. Austenite reversion kinetics are normally divided into three stages. In the first stage (negligible partitioning local equilibrium, NPLE), austenite fraction increases rapidly controlled by carbon diffusion. In the second stage (partitioning local equilibrium first stage, PLE-1), the growth of austenite is controlled by the slow diffusion of substitutional elements in martensite. Finally, in the third stage (partitioning local equilibrium second stage, PLE-2), which is much slower than the previous stages, the austenite growth is controlled by the diffusion of substitutional elements in austenite. Ding *et al.*^[21] found that these stages were not affected by the presence of pre-existing austenite. In addition, they observed that the transition from PLE-1 to PLE-2 occurred after 600 seconds approximately for a Fe–0.2C–8Mn–2Al steel. Wei *et al.*,^[38] instead, estimated that this transition occurred after almost 2000s for a Fe–0.1C–3Mn–1.5Si steel. The kinetics of ART in the Mn and MnNi steels were simulated by means of DICTRA (details of simulation are explained later), obtaining the migration distance of the austenite/ferrite interface and the corresponding austenite content as function of time, which is shown in Figure 11 for the QT10 condition. Although the austenite percentages obtained by DICTRA are quite higher than those measured experimentally by XRD (Figure 4) and calculated from dilatometry results (Figure 3), simulations helped in the understanding of which transformation mode was occurring at each Pt. With a Pt of 300 seconds, austenite reversion kinetics seemed to be in the PLE-1 stage. During this stage the austenite content was still growing, but the reverted austenite amount formed so far led to a relatively high amount of RA. Figure 3 shows that the reversion

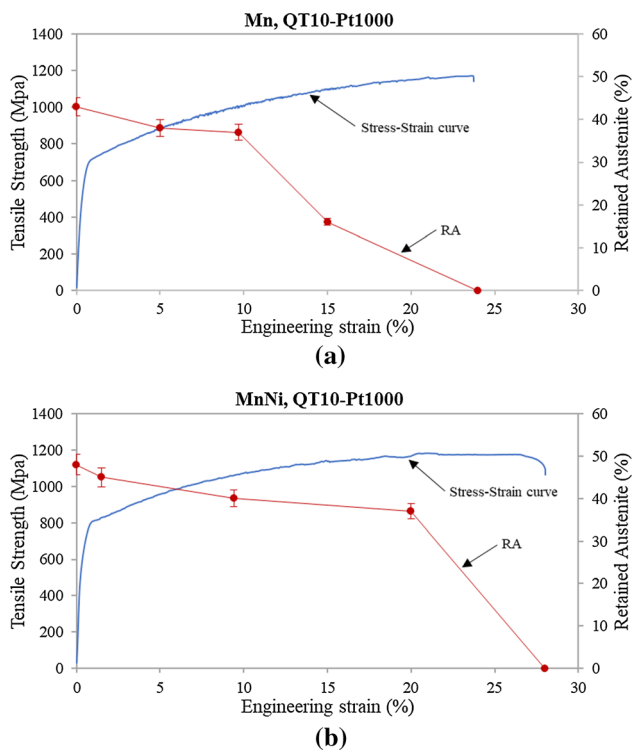


Fig. 10—Engineering stress–strain curves obtained for the QT10–Pt1000 condition and RA measured at different strains for the Mn (a) and MnNi (b) steels.

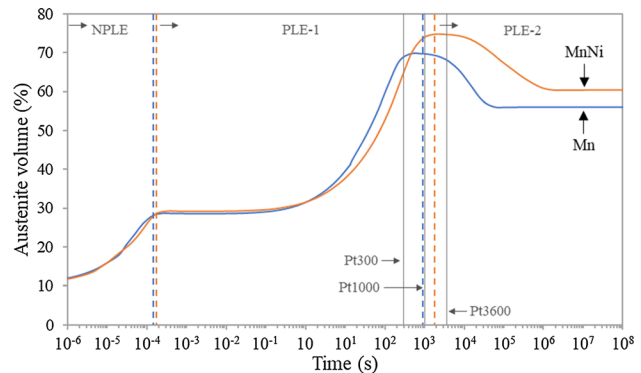


Fig. 11—DICTRA simulations of the austenite reversion kinetics for the QT10 condition.

kinetics of the Mn steel are slightly faster than those of the MnNi steels, which is in agreement with DICTRA simulations, where the transition from PLE-1 to PLE-2 occurred after 900 and 1800s in the Mn and MnNi steels, respectively. Thus, by 1000 seconds of partitioning the growth of austenite was slowed and it is likely that the kinetics were at the beginning of the PLE-2 and at the end of the PLE-1 stage in the Mn and MnNi steels, respectively. Reverted austenite was not far from its maximum and thus outstanding values of RA were obtained in this condition. Finally, at 3600 seconds of partitioning, the controlling kinetics were likely already in the PLE-2 stage and no increase of austenite fraction occurred, leading to the slight decrease of RA measured by XRD.

From a chemical point of view, a large difference in austenite stability is not expected between the Pt1000 and Pt3600 treated steels. However, in FE-SEM microstructures (Figures 5(d) and (e)) a coarsening of RA laths was observed. This behavior was hypothesized to occur due to the coalescence of austenite grains during growth.^[39] As mentioned above,^[37] grain size might influence the thermal stability of austenite, which can explain the slight decrease in RA measured in Pt3600 cycles in comparison with Pt1000 cycles, where thinner RA was observed.

B. Influence of Ni on Austenite Stabilization

The addition of Ni in the MnNi steel was beneficial for increasing RA content in the final microstructure in all heat treatment conditions. The Ni addition did not seem to affect significantly the austenite formation kinetics (as denoted by the similar contraction observed in the partitioning stage, Figures 2 and 3). However, Ni was effective in stabilizing a higher content of austenite. The latter could be related to an enrichment of austenite not only with Mn, but also with Ni. The behaviour of Ni partitioning was analyzed based on compositional maps and concentration profiles shown in Figure 7. In the QT10 condition, some redistribution of Ni can be appreciated in the compositional map (Figure 7(f)), although it was not as distinctive as in the Mn map. However, the concentration profile was very similar to that shown by Mn (Figure 7(h)), with areas enriched in Ni (apparently RA) and areas depleted in Ni (identified as martensite), in the same positions as in the Mn profile. Thereby, the QT10 condition also seemed favourable for Ni partitioning. In the case of the QT25 condition, the Ni partitioning behaviour was less clear and would require further investigation.

The composition of carbides in Ni containing steels was studied in recent work. Pierce *et al.*^[40] observed plate-like and globular carbides in TEM after partitioning at 450 °C for 300 seconds in a 0.2C–1.5Mn–1.3Si steel containing 1.5 pct Ni. Atom probe tomography (APT) revealed Mn enrichment of the carbides. They did not observe significant partitioning of Ni between carbide and matrix, similar to the work of Clarke *et al.*,^[41] who reported no substantial partitioning of Ni between the matrix and the carbide in 4340 steel during tempering at 450 °C for 2 hours. However, Clarke *et al.*

showed via APT that significant rejection of Ni from carbides occurred during tempering at 575 °C for 2 hours, with Ni enrichment persisting near the carbide/ferrite interface. In the present work, the morphology of carbides observed by FE-SEM and TEM was globular and acicular/plate-like in both steels, as also observed by Pierce *et al.*^[40] According to References 42 through 45 acicular carbides nucleate within martensite laths and could be either transitional carbides or cementite. On the other hand, spherical carbides, which are bound to nucleate at triple junctions or prior austenite grains, are likely cementite.^[46,47] Compositional mapping in an area examined in the MnNi steel after the QT10–Pt1000 cycle, which contained both globular and acicular carbides, revealed the enrichment of both types of carbides with Mn (Figure 12(a)). The formation of Mn-containing carbide results in less C and Mn available for austenite stabilization. In addition, to investigate if carbides were Ni-enriched, a line scan was obtained across two globular carbides in the QT10–Pt1000 condition for the MnNi steel (Figure 12(c)). Both carbides contained a high amount of Mn, but no Ni enrichment was evident in the carbides or near the carbide/matrix interfaces.

C. Theoretical Analysis of Austenite Stabilization Using DICTRA

As shown earlier, the ART occurs in the high partitioning temperature stage and Mn partitioning from martensite into austenite was observed in TEM–EDS scans. The Mn concentration profiles were different depending on the QT condition. Furthermore, a substantial carbide fraction was observed, which contained a significant Mn content. According to recent studies,^[45,48–50] austenite is likely to nucleate at carbide interfaces. Therefore, austenite formation could be the result of the growth of pre-existing austenite along with formation of new austenite at carbide interfaces. With the aim of better understanding these possible phenomena, DICTRA simulations were performed for the MnNi steel. In the simulations, two different set ups were considered. In the first one, the growth of pre-existing austenite in the austenite/martensite microstructures was simulated. In the second one, austenite nucleation at carbide interfaces was simulated. In both set ups, a single cell planar geometry was used.^[51] Because of symmetry, only the half thickness was considered in the DICTRA calculation domain. In set up (1), 10 and 25 vol pct of austenite (QT10 and QT25 conditions, respectively) were considered in the initial austenite/martensite microstructure. The dimension of the martensite was set to 0.200 μm . It was based on the TEM observations of Krauss *et al.*, indicating that most martensitic lath widths range from approximately 0.150 to 0.200 μm ,^[52,53] which seems consistent with the TEM analysis presented in this work. Corresponding austenite dimensions were obtained using the “constant ferrite width approach”.^[54] Considering 10 and 25 vol pct of austenite (QT10 and QT25 conditions, respectively), austenite initial lath widths equal to 0.22 or 0.66 μm were fixed. The initial composition of both

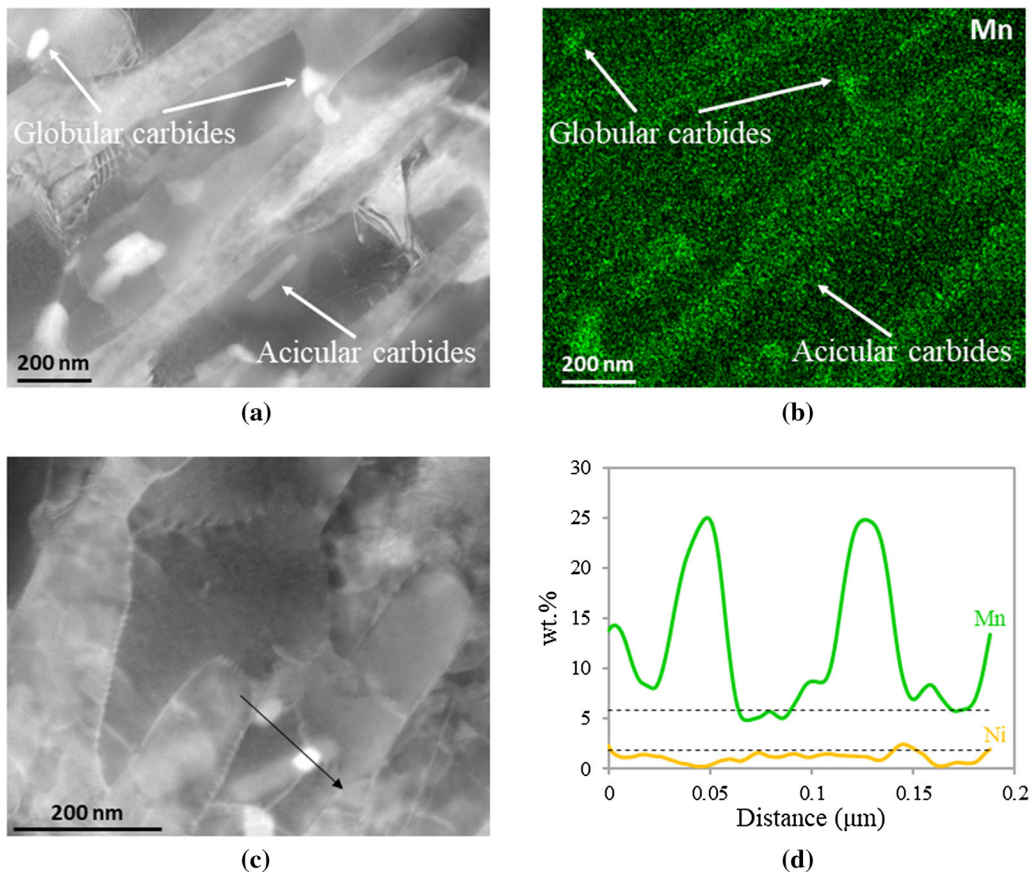


Fig. 12—TEM micrographs (a) and (c); compositional mapping of Mn in MnNi steel after the QT10–Pt1000 thermal cycle (b); and line scans of Mn and Ni concentration (d) corresponding to the line shown in (c). In the micrograph (a), acicular and globular carbides are visible; in the compositional map (d) a higher concentration of Mn is visible in the globular and acicular carbides.

austenite and martensite was the bulk composition. In the case of the QT10 condition, different Pts were considered. A schematic illustration of these initial conditions is shown in Figure 13(a). The results of the simulations were the evolution of austenite growth and concentration profiles of Mn and Ni, which are presented for different QT and Pt conditions in Figures 13(b) and (d), and Figures 13(c) and (e), respectively. In set up (2), the average carbide size and Mn composition measured from TEM analysis were employed, $0.020\ \mu\text{m}$ and 24.6 wt pct, respectively. The partitioning dimension in martensite was set to $0.200\ \mu\text{m}$, as in set up (1). For the MnNi steel at $640\ ^\circ\text{C}$, the ortho-equilibrium predicted by ThermoCalc was a mixture of ferrite and austenite phases. Thus, the initial composition of the martensite was considered from the ortho-equilibrium composition of the ferrite phase (*i.e.*, 0.003 C wt pct and 1.998 Mn wt pct). In addition, in order to simplify the simulation, the nucleation process was ignored, adding a $0.001\ \mu\text{m}$ length austenite phase, with the same composition as the martensite, between the cementite and martensite phases. The initial conditions for this set up are shown in Figure 14(a) and the obtained results are shown in Figure 14(b).

In set up (1), pre-existing austenite grew into the initial martensite lath and was enriched considerably in Mn, while the martensite was considerably depleted in Mn, almost reaching the equilibrium value (Figure 13(b)). With regard to Ni, it can be seen that, the austenite was partially enriched, and the martensite was partially depleted. However, the 1000 seconds Pt condition was not enough time to reach the equilibrium composition. Furthermore, the distribution of the Ni in the austenite was quite heterogeneous (Figure 13(d)). Regarding the influence of QT, the DICTRA calculations appear to be in good agreement with the dilatometry results, where it was seen that the QT10 condition led to a greater amount of reverted austenite formation (Figure 3). According to Figures 13(b) and (d), after 1000 seconds at the Pt, the austenite lath size grew more in the QT10 condition, obtaining a final length 7.5 times the initial one, whereas for the QT25 condition the size was only 3.0 times the initial. With regards to Mn diffusion distance, the enriched width was quite similar for both QT conditions. However, the percentage of the lath size enriched in Mn was greater for the QT10 than the QT25 condition, specifically 78 and 60 pct austenite was enriched in the QT10 and the QT25, respectively. These percentages were somewhat lower regarding Ni

Initial conditions for set up (1)

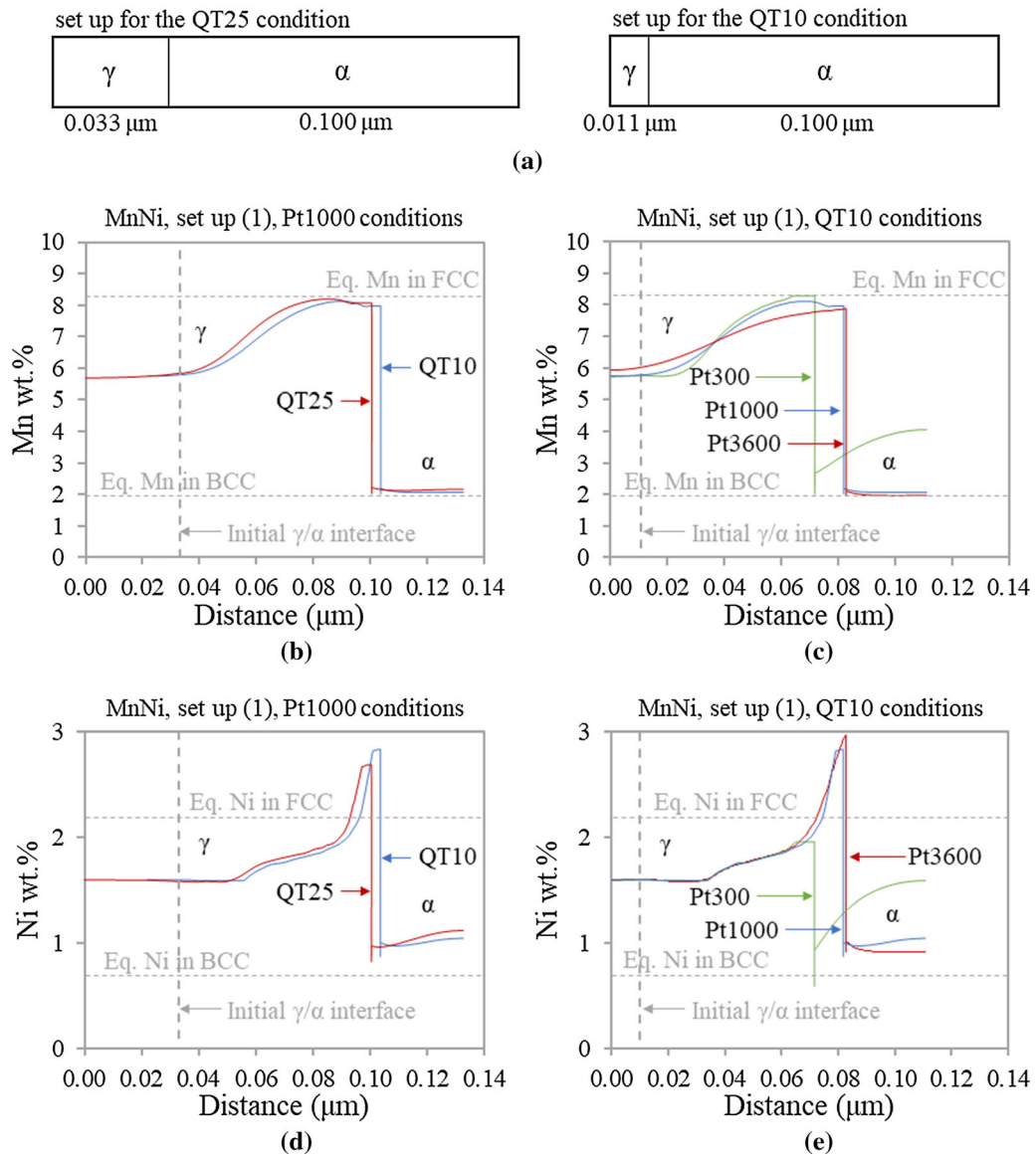


Fig. 13—DICTRA simulations for MnNi steel at 640 °C: schematic of the initial conditions of the simulations for set up (1) (a); results for set up (1) configuration, showing a comparison between the growth of austenite in QT10 and QT25 with Pt1000 and concentration profiles of Mn (b) and Ni (d) (the initial interface was set in the same position for QT10 and QT25); and showing the comparison between the growth of austenite with Pt300, Pt1000, and Pt3600 in QT10 and concentration profiles of Mn (c) and Ni (e).

diffusion distance, specifically 61 and 50 pct in the QT10 and the QT25, respectively. These observations were consistent with TEM–EDS line scans (Figures 7(g) and (h)), and would imply that the quantity of secondary martensite formed in the QT25 condition during final cooling would be higher.

Calculations for different Pts, employing QT10, are shown in Figures 13(c) and (e). As expected, the growth of the austenite was greater with increased Pt, as the interface was moved to longer distances. The growth increment difference with increasing Pt from 300 to 1000 seconds was substantially larger than increasing it from 1000 to 3600 seconds, although in these DICTRA simulations the aforementioned coalescence phenomenon was not considered. At Pt300, there was a

clear distinction between the lath region enriched in Mn and the non-enriched region, which might lead to some secondary martensite formation. In addition, the martensite lath was not completely Mn depleted. At Pt1000, Mn was more homogeneously distributed across the lath, but there was still a small unenriched length, while at Pt3600 the entire length was somewhat enriched, although a compositional difference within the lath was still visible and, thereby, the less enriched part of the lath would potentially transform into secondary martensite. Regarding Ni diffusion, the unenriched austenite length was the same for the three Pt conditions. However, the Ni distribution within the lath was different. At Pt300, the Ni enrichment/depletion in the austenite and martensite, respectively, was poor and

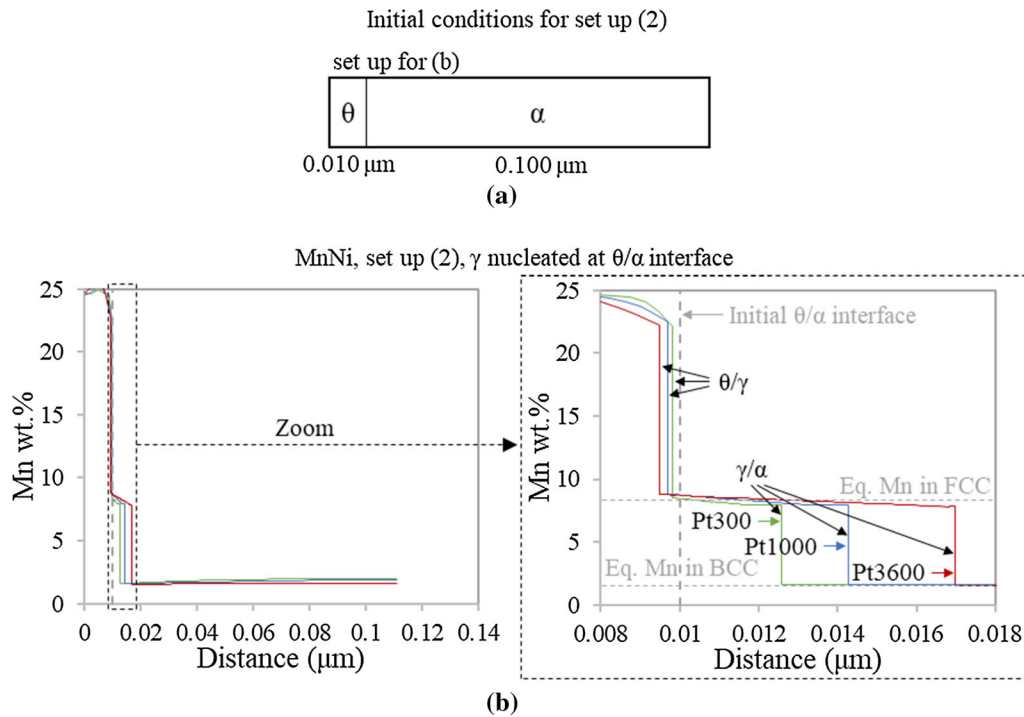


Fig. 14—DICTRA simulations for MnNi steel at 640 °C: schematic of the initial conditions of the simulations for set up (2) (a), and results for set up (2) configuration, where austenite nucleated at the θ/α interface (b).

very localized near the interface. At Pt1000, the Ni enrichment in the austenite continued to be located near the interface, but the peak maximum was above the equilibrium composition. The Ni depletion in the martensite led to a homogeneous distribution, although the content was still beyond the equilibrium value. Finally, at Pt3600, the behavior was like at Pt1000, obtaining a slightly higher Ni enrichment in the austenite near the interface.

In set up (2), different austenite sizes and Mn profiles were obtained when comparing with set up (1). First, the Mn content across the austenite lath was almost constant and very close to the equilibrium content (8.4 wt pct). Second, the austenite lath size was significantly smaller than the size obtained in set up (1), specifically, the total size of the lath after 3600 seconds of partitioning did not reach 0.008 μm , with even lower values after 1000 and 300 seconds, 0.005 and 0.003 μm , respectively. In addition, according to DICTRA calculations, the austenite grew into the martensite rather than dissolving the cementite. Yan *et al.*^[55] also observed that the lath size of austenite was much smaller when it nucleated at the interface between cementite and martensite than when it nucleated at the boundary of the martensite. However, they did not have pre-existing austenite in their simulations and they found that carbides were totally dissolved after holding for 2000s at the intercritical temperature. Additionally, Luo *et al.*^[56] suggested that the dissolution of cementite and the limited diffusion distance of Mn are the main reasons for enriching the Mn concentration and refining the grain size of austenite.

In general, Mn contents measured experimentally in RA (Figures 7(g) and (h)) were somewhat higher than those obtained by DICTRA. On the other hand, in DICTRA simulations, the width enriched in Mn was less than observed, as in both QT conditions it was less than the enriched size measured by TEM–EDS scans. Furthermore, such size without enrichment would lead to a quite higher extent of secondary martensite transformation than that observed by dilatometry. This means that DICTRA calculations could underestimate Mn diffusion through the austenite. In the simulations, ferrite was considered instead of martensite, since martensite is not included in the thermodynamic and kinetic database. The thermodynamic properties of martensite are very much the same as those of ferrite, however, the kinetic parameters may deviate between the two phases due to larger numbers of lattice defects, particularly dislocations, in martensite. Thus, mobilities of all alloying elements in martensite are increased compared to ferrite,^[57] which could explain the differences between the simulations and experimental data.

D. Relationship Between Microstructure and Tensile Properties

As can be seen in Table V, in general, the better tensile properties were obtained with the MnNi steel in the QT10 conditions, except for TS, which was higher after the application of the QT25–Pt1000 cycle. For the MnNi steel, the properties did not deteriorate with the increase of the Pt, whereas in the Mn steel YS and TEL decreased for the Pt of 3600 seconds. The product of TS

and TEL is a parameter often applied to evaluate and compare steels for the automotive sector. In Figure 15, $TS \times TEL$ is represented as a function of RA. It can be seen that outstanding values of $TS \times TEL$ were obtained for the QT10 condition, with the MnNi steel exhibiting higher values. Except for QT10–Pt300 in the Mn steel, it can be said that the product $TS \times TEL$ increased with the RA content. Thus, the presence of a higher content of RA in Ni containing steel and after the QT10 condition, likely contributed to the higher $TS \times TEL$ values. The finer RA laths for the QT10 condition likely played an important role in improving the $TS \times TEL$ product,^[58,59] while the greater amount of secondary martensite reduced the ductility for the QT25 condition.

The presence of secondary martensite can be considered further, as it can be critical for the deterioration of tensile properties.^[21] Even though secondary martensite transformation was difficult to detect by dilatometry for some of the conditions, a deeper analysis allows an approximation of the amount of each constituent in the

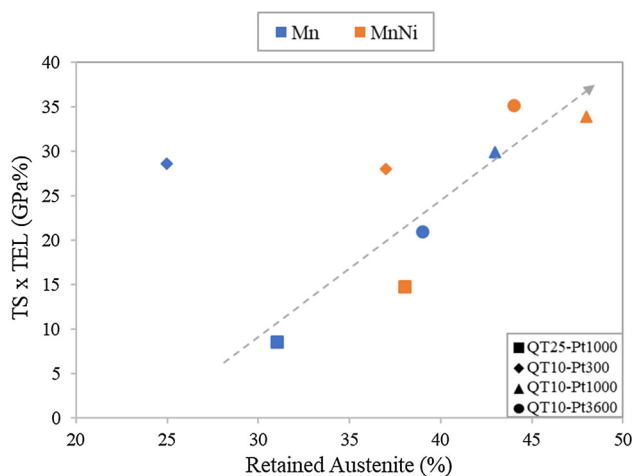


Fig. 15—Graphical representation of the relationship between the product of tensile strength and TEL and RA for each Q&P cycle of both steels.

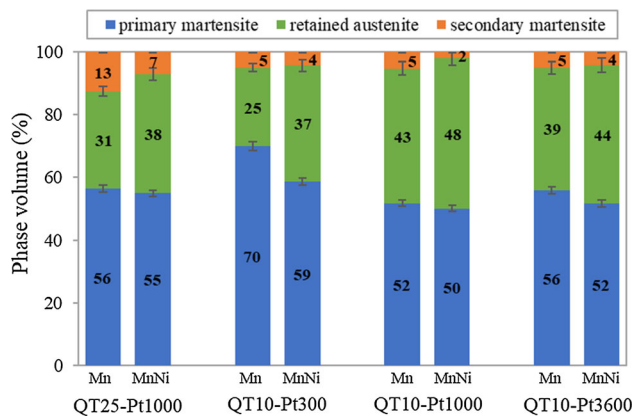


Fig. 16—Volume percent of each phase in both steels after the application of Q&P cycles calculated based on dilatometry curves and RA measured by XRD.

final microstructure. Thus, employing the methodology utilized in Reference 20, the volume fraction of the phases existing in the final microstructure after heat treatments was estimated employing RA measurements (XRD) and dilatometry curves (Figure 16). From the graph, it can be confirmed that the greatest content of secondary martensite was obtained after the QT25–Pt1000 cycle, particularly in the Mn steel. The presence of a hard and brittle secondary martensite in this condition can explain the lower TEL and higher TS obtained after the QT25–Pt1000 cycle.

It is widely accepted that the transformation of austenite into martensite induced by deformation is also a critical factor that determines tensile properties. In both steels, little austenite transformation occurred up to 10 pct strain, where only about 15 pct of the RA had transformed (Figure 10). Afterwards, the behavior was rather different in each steel. In the Mn steel the RA content gradually decreased with strain, whereas in the MnNi steel the entirety of the remaining RA at 20 pct strain (77 pct of the initial RA) transformed close to the uniform strain, likely resulting in a high fraction of very hard martensite and thus provoking early fracture and the absence of post-uniform elongation. Although the Mn steel showed a more gradual decrease in the RA content, it is likely the amount of martensite transformed at strains close to the uniform elongation was still high and also provoked the absence of post-uniform elongation. Therefore, adding Ni increased the mechanical stability of RA and retarded the kinetics of the strain-induced martensite transformation. According to Hidalgo *et al.*^[60] the strength of martensite can affect the mechanical stability of austenite. They concluded that austenite surrounded by a stronger martensitic matrix was mechanically more stable than that surrounded by a weaker martensite. In the present work, Ni decreased the M_s temperature, so the martensite formed during the first cooling to QT should contain more dislocations and, thus, it was likely harder and contributed to the higher mechanical stability of austenite in this steel.^[61]

Stress–strain curves in Figure 8 indicated discontinuous yielding in QT10–Pt1000 and Pt3600 cycles, but not so in the shorter-time Pt300 condition. Raabe *et al.*^[59] recently reviewed different mechanisms contributing to the occurrence of discontinuous yielding. They observed that in some materials such as pure Al, austenitic steels and interstitial-free (IF) steels which normally show a continuous yielding behavior, discontinuous yielding becomes prevalent when their grain sizes are reduced to an ultrafine level. In the present work, a very fine ferrite/austenite microstructure was observed by TEM characterization after the QT10–Pt1000 cycle in the Mn and MnNi steels, as well as a large amount of RA, as in medium Mn steels (Figure 7), which might help explain this discontinuous yielding.^[62,63] In the case of the Pt300 cycle, a shorter partition time led to less tempered martensite and, therefore, a higher density of mobile dislocations, resulting in the continuous yielding observed in the stress–strain curves of the QT10–Pt300 condition. In the case of the QT25, the presence of higher secondary martensite amounts might explain the continuous yielding in the same way.

V. CONCLUSIONS

Q&P cycles with a high partitioning temperature, in which the ART phenomenon occurred, were investigated in a medium Mn steel and a medium Mn steel containing Ni. The following conclusions were drawn:

- (1) Large amounts of RA were obtained in the final microstructure, which were comparable to those obtained after intercritical annealing of medium Mn steels. The addition of Ni further increased the content of RA. The presence of pre-existing austenite (due to interrupted quenching) before the partitioning stage considerably reduced the Pt in comparison with some conventional intercritical annealing heat treatments of medium Mn steel.
- (2) A lower QT resulted in faster austenite formation kinetics in the partitioning stage, less formation of secondary martensite in the final cooling, and a final microstructure with a higher content of RA, which showed a lath-type microstructure with finer constituents.
- (3) After the Q&P cycles, Mn and Ni enriched RA laths were observed. The enrichment of Mn was different depending on the QT condition. In the lower QT condition, the partitioning of substitutional elements was more homogeneous due to the thinner austenite laths. The partitioning of Ni was also observed. In the higher QT condition, Mn was concentrated near the MA interface.
- (4) Carbides with globular and acicular/plate-like morphologies and containing Mn were formed in the high partitioning temperature cycles, which left less C and Mn available for partitioning.
- (5) The mechanical stability of the RA was enhanced by the addition of Ni. In the MnNi steel, austenite transformation was very modest up to 20 pct strain. However, very abrupt austenite transformation occurred above this strain level, resulting in high fraction of strain-induced martensite. In the Mn steel, RA transformed more gradually, but still resulting in the important quantity of strain-induced martensite at high strain levels. Therefore, the tensile curves of both steels showed very small or inexistent post-uniform elongation.

ACKNOWLEDGMENTS

This research is partially funded by the European Commission in the HIGHQP Project, which has received funding from the Research Fund for Coal and Steel under Grant Agreement No 709855. This study reflects only the author's views and the European Commission is not responsible for any use that may be made of the information contained therein. The authors thank for technical and human support provided by SGIker (UPV/EHU/ERDF, EU). The

authors also acknowledge the support of the sponsors of the Advanced Steel Processing and Products Research Center.

CONFLICT OF INTEREST

The authors declare that they have no conflict of interest.

OPEN ACCESS

This article is licensed under a Creative Commons Attribution 4.0 International License, which permits use, sharing, adaptation, distribution and reproduction in any medium or format, as long as you give appropriate credit to the original author(s) and the source, provide a link to the Creative Commons licence, and indicate if changes were made. The images or other third party material in this article are included in the article's Creative Commons licence, unless indicated otherwise in a credit line to the material. If material is not included in the article's Creative Commons licence and your intended use is not permitted by statutory regulation or exceeds the permitted use, you will need to obtain permission directly from the copyright holder. To view a copy of this licence, visit <http://creativecommons.org/licenses/by/4.0/>.

SUPPLEMENTARY INFORMATION

The online version of this article (<https://doi.org/10.1007/s11661-022-06796-x>) contains supplementary material, which is available to authorized users.

REFERENCES

1. J. Speer, D.K. Matlock, B.C. De Cooman, and J.G. Schroth: *Acta Mater.*, 2003, vol. 51, pp. 2611–22.
2. N. Foston: *Advanced High Strength Sheet Steels*, Springer, Cham, 2015.
3. J. Mola and B.C. De Cooman: *Metall. Mater. Trans. A*, 2013, vol. 44A, pp. 946–67.
4. M.J. Santofimia, L. Zhao, R. Petrov, C. Kwakernaak, W.G. Sloof, and J. Sietsma: *Acta Mater.*, 2011, vol. 59, pp. 6059–68.
5. E. De Moor, J.G. Speer, D.K. Matlock, J.H. Kwak, and S.B. Lee: *ISIJ Int.*, 2011, vol. 51, pp. 137–44.
6. M.J. Merwin: *Proc. AIST Steel Prop. Appl. Conf.*, Detroit, 2007, pp. 67–84.
7. R.L. Miller: *Metall. Trans.*, 1972, vol. 3, pp. 905–12.
8. T. Furukawa: *Mater. Sci. Technol. (U.K.)*, 1989, vol. 5, pp. 465–70.
9. P.J. Gibbs, E. De Moor, M.J. Merwin, J.G. Speer, and D.K. Matlock: *Metall. Mater. Trans. A*, 2011, vol. 42A, pp. 3691–3702.
10. A. Arlazarov, M. Gouné, O. Bouaziz, A. Hazotte, G. Petitgand, and P. Barges: *Mater. Sci. Eng. A*, 2012, vol. 542, pp. 31–39.
11. D.E. Kim, Y.K. Park, O.Y. Lee, K.G. Jin, and S.J. Kim: *Korean J. Mater. Res.*, 2005, vol. 15, pp. 115–20.
12. J. Shi, X. Sun, M. Wang, W. Hui, H. Dong, and W. Cao: *Scripta Mater.*, 2010, vol. 63, pp. 815–18.

13. A. Bhattacharya, P.K. Bokinala, R. Mitra, and D. Chakrabarti: *Mater. Sci. Technol. (U.K.)*, 2019, vol. 35, pp. 55–67.
14. P.J. Du, D.P. Yang, M.K. Bai, X.C. Xiong, D. Wu, G.D. Wang, and H.L. Yi: *Mater. Sci. Technol. (U.K.)*, 2019, vol. 35, pp. 2084–91.
15. J.G. Speer, R.E. Hackenberg, B.C. Decooman, and D.K. Matlock: *Philos. Mag. Lett.*, 2007, vol. 87, pp. 379–82.
16. G.A. Thomas and J.G. Speer: *Mater. Sci. Technol. (U.K.)*, 2014, vol. 30, pp. 998–1007.
17. D. De Knijf, M.J. Santofimia, H. Shi, V. Bliznuk, C. Föjer, R. Petrov, and W. Xu: *Acta Mater.*, 2015, vol. 90, pp. 161–68.
18. E.J. Seo, L. Cho, and B.C. De Cooman: *Acta Mater.*, 2016, vol. 107, pp. 354–65.
19. S. Ayenampudi, C. Celada-Casero, J. Sietsma, and M.J. Santofimia: *Materialia*, 2019, vol. 8, 100492.
20. M. Arribas, T. Gutiérrez, E. Del Molino, A. Arlazarov, I. De Diego-Calderón, D. Martin, D. De Caro, S. Ayenampudi, and M.J. Santofimia: *Metals*, 2020, vol. 10, p. 862.
21. R. Ding, Z. Dai, M. Huang, Z. Yang, C. Zhang, and H. Chen: *Acta Mater.*, 2018, vol. 147, pp. 59–69.
22. S. Ayenampudi, Z. Arechabaleta, and M. Arribas: *Metall. Mater. Trans. A*, 2021, vol. 52A, pp. 5–11.
23. E. Del Molino, T. Gutierrez, M. Serna-Ruiz, M. Arribas, and A. Arlazarov: *Mater. Sci. Forum*, 2021, vol. 1016, pp. 379–84.
24. K. Kim and S.J. Lee: *Mater. Sci. Eng. A*, 2017, vol. 698, pp. 183–90.
25. E. De Moor, P.J. Gibbs, J.G. Speer, D.K. Matlock, and J.G. Schroth: *Iron Steel Technol.*, 2010, vol. 7, pp. 133–44.
26. J.G. Speer, F.C. Rizzo Assunção, D.K. Matlock, and D.V. Edmonds: *Mater. Res.*, 2005, vol. 8, pp. 417–23.
27. D.V. Edmonds, K. He, F.C. Rizzo, B.C. De Cooman, D.K. Matlock, and J.G. Speer: *Mater. Sci. Eng. A*, 2006, vol. 438–440, pp. 25–34.
28. S. Suwas and R.K. Ray: *Crystallographic Texture of Materials*, Springer, London, 2014.
29. T. Tsuchiyama, T. Sakamoto, S. Tanaka, and T. Masumura: *ISIJ Int.*, 2020, vol. 60, pp. 2954–62.
30. L. Liu, B.B. He, G.J. Cheng, H.W. Yen, and M.X. Huang: *Scripta Mater.*, 2018, vol. 150, pp. 1–6.
31. B.C. De Cooman, S. Lee, and S.S. Kumar: *Proc. 2nd Int. Conf. "Super-High Strength Steels"*, Italy, 2010, pp. 1–11.
32. S. Lee and B.C. De Cooman: *Metall. Mater. Trans. A*, 2013, vol. 44A, pp. 5018–24.
33. E. De Moor, S. Kang, J.G. Speer, and D.K. Matlock: *Proc. Int. Conf. Min. Mater. Metall. Eng.*, 2014, pp. 1–7.
34. K.W. Andrews: *J. Iron Steel Inst.*, 1965, vol. 203, pp. 721–27.
35. D.P. Koistinen and R.E. Marburger: *Acta Metall.*, 1959, vol. 7, pp. 59–60.
36. M.J. Santofimia, J.G. Speer, A.J. Clarke, L. Zhao, and J. Sietsma: *Acta Mater.*, 2009, vol. 57, pp. 4548–57.
37. A. Arlazarov, M. Gouné, O. Bouaziz, and A. Hazotte: *Philos. Mag. Lett.*, 2017, vol. 97, pp. 125–31.
38. R. Wei, M. Enomoto, R. Hadian, H.S. Zurob, and G.R. Purdy: *Acta Mater.*, 2013, vol. 61, pp. 697–707.
39. T. Shinozaki, Y. Tomota, T. Fukino, and T. Suzuki: *ISIJ Int.*, 2017, vol. 57, pp. 533–39.
40. D.T. Pierce, D.R. Coughlin, K.D. Clarke, E. De Moor, J. Poplawsky, D.L. Williamson, B. Mazumder, J.G. Speer, A. Hood, and A.J. Clarke: *Acta Mater.*, 2018, vol. 151, pp. 454–69.
41. A.J. Clarke, M.K. Miller, R.D. Field, D.R. Coughlin, P.J. Gibbs, K.D. Clarke, D.J. Alexander, K.A. Powers, P.A. Papin, and G. Krauss: *Acta Mater.*, 2014, vol. 77, pp. 17–27.
42. S. Yan, X. Liu, W.J. Liu, H. Lan, and H. Wu: *Mater. Sci. Eng. A*, 2014, vol. 620, pp. 58–66.
43. F. HajyAkbar, J. Sietsma, G. Miyamoto, T. Furuhashi, and M.J. Santofimia: *Acta Mater.*, 2016, vol. 104, pp. 72–83.
44. F. HajyAkbar, J. Sietsma, G. Miyamoto, N. Kamikawa, R.H. Petrov, T. Furuhashi, and M.J. Santofimia: *Mater. Sci. Eng. A*, 2016, vol. 677, pp. 505–14.
45. J.J. Mueller, X. Hu, X. Sun, Y. Ren, K. Choi, E. Barker, J.G. Speer, D.K. Matlock, and E. De Moor: *Mater. Des.*, 2021, vol. 203, 109598.
46. H.R. Ghazvinloo, A. Honarbakhsh-Raouf, and E. Borhani: *Metallurgist*, 2016, vol. 60, pp. 758–64.
47. H. Luo, J. Liu, and H. Dong: *Metall. Mater. Trans. A*, 2016, vol. 47A, pp. 3119–24.
48. Z.J. Xie, G. Han, Y.S. Yu, C.J. Shang, and R.D.K. Misra: *Mater. Charact.*, 2019, vol. 153, pp. 208–14.
49. J. Teixeira, M. Moreno, S.Y.P. Allain, C. Oberbillig, G. Geandier, and F. Bonnet: *Acta Mater.*, 2021, vol. 212, 116920.
50. F. Huyan, J.Y. Yan, L. Höglund, J. Ågren, and A. Borgenstam: *Metall. Mater. Trans. A*, 2018, vol. 49A, pp. 1053–60.
51. A. Borgenstam, A. Engstro, L. Ho, and J.A. Gren: *J. Phase Equilib.*, 2000, vol. 21, pp. 269–80.
52. C.A. Apple, R.N. Caron, and G. Krauss: *Metall. Trans.*, 1974, vol. 5, pp. 593–99.
53. T. Swarr and G. Krauss: *Metall. Trans. A*, 1976, vol. 7, pp. 41–48.
54. A.J. Clarke: Ph.D. Thesis, Colorado School of Mines, Golden, CO, 2006.
55. N. Yan, H. Di, R.D.K. Misra, H. Huang, and Y. Li: *Mater. Sci. Eng. A*, 2019, vol. 753, pp. 11–21.
56. H. Luo, J. Shi, C. Wang, W. Cao, X. Sun, and H. Dong: *Acta Mater.*, 2011, vol. 59, pp. 4002–14.
57. O. Dmitrieva, D. Ponge, G. Inden, J. Millán, P. Choi, J. Sietsma, and D. Raabe: *Acta Mater.*, 2011, vol. 59, pp. 364–74.
58. P. Gao, W. Chen, F. Li, B. Ning, and Z. Zhao: *Acta Metall. Sin. (Engl. Lett.)*, 2020.
59. D. Raabe, B. Sun, A.K. Da Silva, B. Gault, H.-W. Yen, K. Sedighiani, P.T. Sukumar, I.R. Souza Filho, S. Katnagallu, E. Jägle, P. Kürnsteiner, N. Kusampudi, L. Stephenson, M. Herbig, C.H. Liebscher, H. Springer, S. Zaefferer, V. Shah, S.-L. Wong, C. Baron, M. Diehl, F. Roters, and D. Ponge: *Metall. Mater. Trans. A*, 2020, vol. 51, pp. 5517–86.
60. J. Hidalgo, R.M. Huizenga, K.O. Findley, and M.J. Santofimia: *Mater. Sci. Eng. A*, 2019, vol. 745, pp. 185–94.
61. J. Nishikawa, T. Maki, and S. Morito: *ISIJ Int.*, 2003, vol. 43, pp. 1475–77.
62. J. Galán, L. Samek, P. Verleysen, K. Verbeken, and Y. Houbart: *Rev. Metal.*, 2012, vol. 48, pp. 118–31.
63. J. Zhao, Z. Jiang, and C.S. Lee: *Mater. Sci. Eng. A*, 2013, vol. 562, pp. 144–51.

Publisher's Note Springer Nature remains neutral with regard to jurisdictional claims in published maps and institutional affiliations.